

# TagScan: Simultaneous Target Imaging and Material Identification with Commodity RFID Devices

Ju Wang<sup>†</sup>, Jie Xiong<sup>#</sup>, Xiaojiang Chen<sup>†</sup>,  
Hongbo Jiang<sup>‡</sup>, Rajesh Krishna Balan<sup>#</sup>, Dingyi Fang<sup>†</sup>

<sup>†</sup>Northwest University, <sup>#</sup>Singapore Management University,

<sup>‡</sup>Huazhong University of Science and Technology

<sup>†</sup>{wangju,xjchen,dyf}@nwu.edu.cn, <sup>#</sup>{jxiong,rajesh}@smu.edu.sg, <sup>‡</sup>hongbojiang2004@gmail.com

## ABSTRACT

Target imaging and material identification play an important role in many real-life applications. This paper introduces TagScan, a system that can identify the material type and image the horizontal cut of a target *simultaneously* with cheap commercial off-the-shelf (COTS) RFID devices. The key intuition is that different materials and target sizes cause different amounts of phase and RSS (Received Signal Strength) changes when radio frequency (RF) signal penetrates through the target. Multiple challenges need to be addressed before we can turn the idea into a functional system including (i) indoor environments exhibit rich multipath which breaks the linear relationship between the phase change and the propagation distance inside a target; (ii) without knowing either material type or target size, trying to obtain these two information simultaneously is challenging; and (iii) stitching pieces of the propagation distances inside a target for an image estimate is non-trivial.

We propose solutions to all the challenges and evaluate the system's performance in three different environments. TagScan is able to achieve higher than 94% material identification accuracies for 10 liquids and differentiate even very similar objects such as Coke and Pepsi. TagScan can accurately estimate the horizontal cut images of more than one target behind a wall.

## CCS CONCEPTS

• **Computer systems organization** → **Sensors and actuators**;

## KEYWORDS

Horizontal cut imaging; Material identification; Multipath suppression; Phase and RSS measurements; RFID

Permission to make digital or hard copies of all or part of this work for personal or classroom use is granted without fee provided that copies are not made or distributed for profit or commercial advantage and that copies bear this notice and the full citation on the first page. Copyrights for components of this work owned by others than ACM must be honored. Abstracting with credit is permitted. To copy otherwise, or republish, to post on servers or to redistribute to lists, requires prior specific permission and/or a fee. Request permissions from [permissions@acm.org](mailto:permissions@acm.org).

MobiCom'17, October 16–20, 2017, Snowbird, UT, USA

© 2017 Association for Computing Machinery.

ACM ISBN 978-1-4503-4916-1/17/10...\$15.00

<https://doi.org/10.1145/3117811.3117830>

## 1 INTRODUCTION

Device-free passive sensing, where no device is attached to the target, has recently received considerable attentions. Many compelling applications are enabled by device-free passive sensing, such as human motion tracking [2, 45], gesture and activity recognition [35, 37], elderly fall detection [38], and even localizing a person behind a wall [3, 41]. Diverse technologies have been employed for these applications including camera [48], infrared [18], audio [36] and RF signal [47].

Among the technologies for device-free passive sensing, RF-based approaches [22, 28, 31, 37] offer two appealing advantages: (i) functioning in the dark environments and (ii) RF signals can penetrate non-metal walls. More importantly, RF-based solutions are promising due to their ubiquity and low cost. In particular, RFID is evolving as a major candidate for object identification and localization in indoor environments. RFID has been used for localization [32, 34], baggage sorting [25, 44], gesture recognition [10, 26], and even tracing a user's handwriting in the air without a physical touch screen [16, 33]. RFID tags are everywhere and commonly used for bus cards, car keys, pass cards, etc. One main reason for the widespread of usage is the simplicity and extremely low cost of the RFID tags (each tag costs 5–10 cents USD).

Though a success in localization and gesture recognition, a missing research component of existing device-free sensing technology is using cheap commodity RF devices, such as RFID, to perform target imaging and material identification. Many applications would benefit from knowing the shape and material type of a target. For example, a robot can automatically adjust its grip strength if it knows the object is an egg instead of a stone by using material identification. Detecting concealed weapons at a security checkpoint would be possible by knowing the target shape and the material type. It will be possible to differentiate Pepsi from Coke without labels or a taste test.

Existing target imaging and material identification systems, such as Radar [19], X-Ray [21], CT/MRI [49] and B-scan ultrasonography [7], use dedicated hardware with high frequency signal, large bandwidth and antenna arrays, which are extremely expensive and usually large in size. Moreover, X-Ray and CT employ very high frequency signals which are harmful to the human body [23].

Recently, some researchers attempt to use the RF signals to image a target's shape [1, 8, 11] or identify a target's material [46, 50].

RF-Capture [1] can capture the skeleton of a human target using special-purpose hardware with larger than 1 GHz bandwidth Frequency Modulated Continuous Wave (FMCW) signals. However, commodity Wi-Fi and RFID devices have much smaller bandwidths. Wison system [11] with a two-dimensional antenna array, employs the reflected Wi-Fi signal from the target for imaging. However, its imaging performance is still coarse. Moreover, the above systems employ the reflection signals bounced off the target. Thus, these systems can only obtain the surface image and the surface material of a target – they are not able to obtain the internal horizontal cut image and the internal material of a target. Overall, imaging a target's shape and identifying its material type with cheap commodity devices remain challenging.

This paper introduces TagScan, a system that can both identify the material type and image the internal horizontal cut of a target *simultaneously* with cheap COTS RFID devices. Unlike existing systems which employ dedicated hardware or special-purpose large bandwidth signals to extract the reflectivity and permeability parameters for material identification [40], TagScan exploits the phase and RSS changes when the signal penetrates inside a target for material identification and imaging. The phase and RSS measurements are widely available on commodity devices and TagScan works well with a small 4 MHz bandwidth. We believe this work introduces a new direction for performing material identification and imaging with COTS devices. TagScan's material identification and imaging are based on the key observation that different materials and target sizes will cause different amounts of phase and RSS changes when the RF signal penetrates through a target. Further, if there is no multipath, the phase change values exhibit a linear relationship with the propagation distances inside the target.

Though the basic idea sounds straightforward, it is non-trivial to realize TagScan due to the following challenges:

- **Challenge 1:** In an indoor environment, the rich multipath signals break the linear relationship between the phase changes and the propagation distances inside a target.
- **Challenge 2:** Determining the size of a target given the material type or identifying the material given the target size is relatively easy. Without knowing either material type or target size, trying to identify these two pieces of information at the same time is much more challenging.
- **Challenge 3:** Even if the propagation distances inside a target at different directions are obtained, stitching them together to create the image is still challenging as the starting points of the propagation distances are unknown.

To deal with the first challenge, we propose a multipath suppression scheme based on the following observations: (i) the phase measurements change linearly over the carrier frequencies if the direct-path signal dominates; (ii) for nearby tags and adjacent channels, the direct-path signals are similar while the multipath signals are usually quite different. Based on the first observation, TagScan picks data from relatively “clean” channels that are not greatly affected by multipath for processing. With the second observation, TagScan further reduces the multipath effect by applying carefully chosen weights on the signals received from different tags and at different channels, so that the power of the direct-path signals increases

greatly while the power of the reflection signals is averaged out to a small value.

To address the second challenge, although the RSS change and phase change are dependent on both the target material and the target size, we discover a parameter that related to the ratio of *RSS change* and *phase change* (denoted as RP-rate) is a unique feature for each material type and independent of the target size. By removing one variable, we are able to obtain the target material and size/shape at the same time.

To deal with the third challenge, the key intuition is that the target images estimated from two different arrays will align well when all the starting points of the propagation distances are correctly selected. We thus model the imaging problem as an optimization problem and search the starting points by minimizing the difference of two images estimated from the two arrays.

We build a prototype of TagScan using just one Impinj RFID reader [14] and 16 cheap Alien RFID tags [12]. The 16 tags form two linear tag-arrays with 8 tags in each. We evaluate the material identification and imaging performance in three typical indoor environments: a library, a lab-office and an empty hall corresponding to high, medium and low multipath environments. In the lab-office environment, the material identification accuracies of TagScan are higher than 94% and 91% for 10 types of liquids and 6 types of solid targets, respectively. Note that we employ very similar liquids such as Pepsi, Coke and sweet water with different sugar concentrations to make our material identification problem challenging. TagScan can also estimate the cut image of a human body accurately which has attractive authentication application. In a more challenging scenario, TagScan can estimate the cut images of a cube and a cylinder behind a wall simultaneously when they are not close to each other.

**Contributions:** The main contributions of this paper are summarized as follows:

- (1) To the best of our knowledge, this is the first RFID-based system which utilizes the widely available phase and RSS information on COTS devices to perform material identification and target imaging simultaneously.
- (2) We propose a multipath suppression method so that even in a rich multipath environment, the phase and RSS changes can be used to identify the material type and image the target shape at a high accuracy.
- (3) We discover a feature that is unique for each material type and independent of the target size, and also can be easily calculated from the RSS and phase readings. We observe that this feature is sensitive enough to help differentiate between Pepsi and Coke.
- (4) Without knowing the ground truth image beforehand, TagScan is able to estimate the cut image of a target based on one observation: the images estimated from two different arrays align well if they are estimated correctly.
- (5) We design and implement TagScan with COTS RFID devices. Comprehensive experiments demonstrate the effectiveness of TagScan under varying conditions.

**Paper outline:** We introduce the preliminary studies in Section 2. We detail TagScan's design in Section 3. The implementation is described in Section 4 followed by the evaluations in Section 5. We discuss limitations and other related issues in Section 6. The related work is shown in Section 7 and we conclude this paper in Section 8.

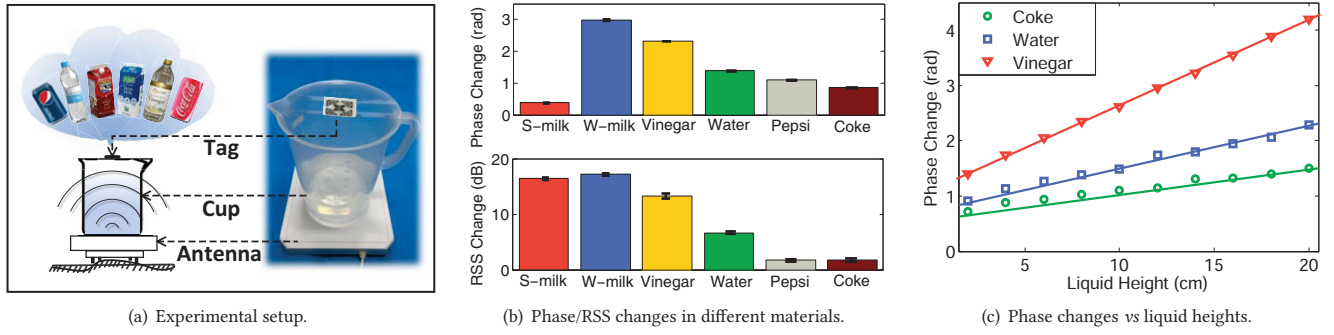


Figure 1: Preliminary studies of the phase and RSS changes inside targets with different materials and different sizes.

## 2 PRELIMINARY

We present the preliminary studies of the phase and RSS changes inside a target and the effect of multipath on the phase change measurements in this section.

### 2.1 Phase Changes Inside a Target

To illustrate TagScan's basic idea for material identification, Fig. 1(a) shows an example where a directional antenna of an RFID reader is placed on the ground in an open space to minimize the amount of multipath. A plastic measuring cup with a height of 28.5 cm and a diameter of 19.7 cm is placed on top of the antenna. We place an RFID tag on top of the cup and pour the same amount (8 cm of height) of purified water, vinegar, skimmed milk, whole milk, Coke and Pepsi into the cup. We measure the phase and RSS readings before and after each liquid is poured into the cup, and then calculate the changes shown in Fig. 1(b).

We observe that the phase changes for water, vinegar, skimmed milk and whole milk are quite different. For Coke and Pepsi, the result is surprising since there is still around 0.2 radians phase change difference,<sup>1</sup> which is clear enough for us to differentiate them. The RSS changes for Coke and Pepsi are very similar but are quite different from other liquids. The observation implies that it is possible to employ the phase and RSS changes for material identification. Note that the commodity RFID reader eliminates the directly reflected signal from a target and only keeps the signal from the tags [14].

To illustrate TagScan's basic idea for imaging, we use three different types of liquids (purified water, Coke, and vinegar) and run the following benchmark experiment. We vary the amount of liquid in the cup and measure the phase changes with respect to the empty cup. During the process, the gap distance between the tag and the liquid surface is decreased from 26.5 cm to from 8.5 cm in a step of 2 cm and the liquid height is increased from 2 cm to 20 cm. Fig. 1(c) shows a clear linear relationship between the phase change and the distance that the signal travelled inside the liquid. Further, the slopes of different materials are distinct. Based on this observation, if the material of a target is known, TagScan can get the propagation distance inside the target with the phase change measurement. This propagation distance is the "width" information of the target at one angle. By stitching those "widths" from many angles, TagScan can obtain the target's cut image.

<sup>1</sup>Impinj R420 reader [14] has an analog to digital converter of 12-bit which achieves a phase resolution of 0.0015 radians.

### 2.2 Phase Changes in Multipath Environment

We show the intuition behind our multipath suppression method using both the theoretical analysis and the benchmark experiments. In an ideal open space without any multipath, the measured phase difference between frequency  $f_p$  and frequency  $f_q$  at a reader can be written as:

$$\Delta\phi_{f_p, f_q} = \frac{4\pi L}{C}(f_p - f_q), \quad (1)$$

where  $C$  is the speed of light and  $L$  is the distance between the tag and antenna. Since  $L$  is a constant for a given deployment, the slope  $4\pi L/C$  of the phase change is also a constant. So the phase value changes linearly with frequency when there is only direct path. In reality, the linear relationship is broken by multipath. We run benchmark experiments in three different environments: a hall environment (little multipath), a lab-office environment (medium multipath), and a library environment (rich multipath). An RFID tag is placed 5 m away from the reader antenna, and the reader is programmed to hop over 16 adjacent channels.<sup>2</sup>

**Observation 1:** Fig. 2 shows the phase measurements over 16 channels in four different environments with different amounts of multipath. We can see that in the hall environment with little multipath, the linear relationship between phases and channels can still be observed. One reason behind this is that commodity RFID devices usually employ directional antennas to increase the transmission range, which reduces the amount of multipath. However, even with directional antenna, in a rich-multipath environment such as a library, the linear relationship does not exist any more.

**Observation 2:** Fig. 3 shows the phase measurements of 6 nearby tags (the spacing between adjacent tags is about 10 cm) in the hall environment. We can see that the slopes of the phase changes are similar for closely placed tags. As direct path is dominant in the hall environment, we conclude that the direct-path signals are similar at closely placed tags.

These results convince us to select phase readings from the relatively "clean" channels based on the linear property when multipath is not strong. The selection pool is large as we have multiple tags and each tag has multiple channels. When multipath is strong, it is difficult to find these kind of "clean" channels and thus we propose a multipath suppression scheme (Section 3.2) to address the multipath issue.

<sup>2</sup>The frequency range of Impinj R420 reader in China is 920.625 ~ 924.375 MHz and each channel has a bandwidth of 250 KHz.

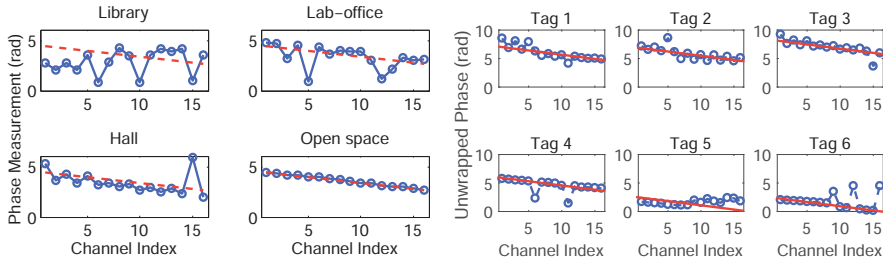


Figure 2: Phase changes linearly when the direct-path signal dominates.

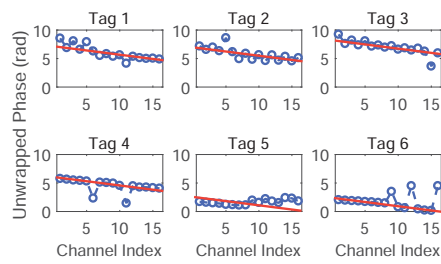


Figure 3: Unwrapped phase data over 16 channels in the hall environment.

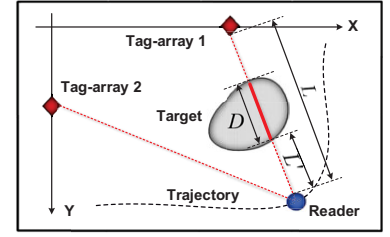


Figure 4: An overview of TagScan's system deployment setup.

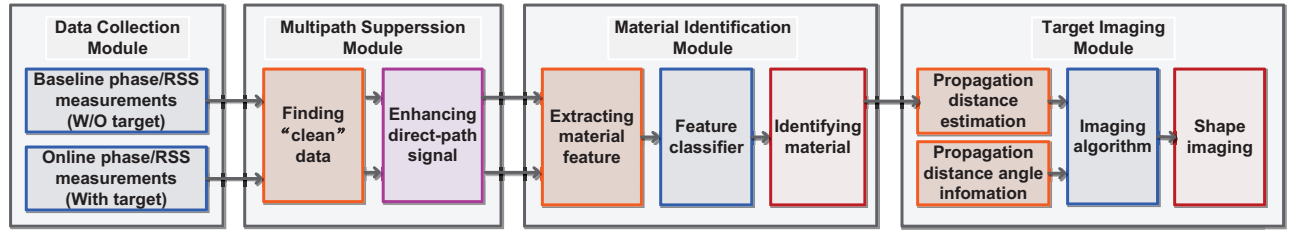


Figure 5: System architecture of TagScan.

### 3 DESIGN

#### 3.1 Overview

TagScan is a material identification and imaging system built on COTS RFID devices. It only uses one RFID reader with one antenna and multiple tags which form two linear tag-arrays as shown in Fig. 4. The reader communicates with the tags across different frequency channels.<sup>3</sup> For imaging, we let the reader move along a given trajectory. When the target blocks the direct path between the reader and tag-array, phase and RSS changes can be observed and are utilised for material identification and target image. Fig. 5 shows the system architecture which has four modules:

- **Data Collection Module:** TagScan collects a set of phase and RSS measurements as the baseline data<sup>4</sup> when there is no target. TagScan then acquires another set of measurements when the target appears.
- **Multipath Suppression Module:** TagScan first identifies the relatively “clean” channels which are not greatly affected by multipath. TagScan then strengthens the power of the direct-path signal and reduces the power of reflection signals by assigning carefully chosen weights to the measured signals at different channels and different tags as discussed in Section 3.2.
- **Material Identification Module:** TagScan extracts the feature parameter *RP-rate* which is only dependent on the target material and employs the “K Nearest Neighbor” (KNN) [9] classifier to identify the target’s material as described in Section 3.3. Note that for material identification, only one tag-array is needed and the reader does not need to move.
- **Target Imaging Module:** Once the target material is identified, TagScan estimates the signal propagation distance inside the target along a specific direction. This propagation distance is the

“width” information of the target at one angle. TagScan stitches together the “widths” from many angles to obtain the horizontal cut image of the target as described in Section 3.4.

#### 3.2 Multipath Suppression

TagScan relies on the linear relationship between the distance travelled inside the target and the phase/RSS changes for material identification and target imaging. However, multipath reflections break the linear relationship. To deal with multipath, we introduce a two-stage multipath suppression method. In stage 1, we identify the relatively “clean” channels that are not greatly affected by multipath. In stage 2, we further reduce the effect of multipath by assigning carefully chosen weights to the measured signals at different channels and different tags. By doing this, the power of direct-path signals increases greatly while the power of the reflection signals is averaged out to a small value.

**3.2.1 Identifying the relatively “clean” channels.** Using “Observation 1” and “Observation 2” in Section 2.2, we identify the relatively “clean” channels whose direct-path signal dominates with a simple linear fit. However, this works well only in the environment with little multipath such as the hall environment and is much less reliable in medium and rich multipath environments.

**3.2.2 Enhancing the direct-path signal.** Using the method described above, we are able to remove “dirty” data in environments with little multipath. However, there is always residual multipath noise left in the relatively “clean” data. Furthermore, in a rich multipath environment, it is difficult to identify such “clean” channels. Thus, we propose a method to strengthen the direct-path signal and reduce the power of multipath reflection signals.

At a high level, we combine signals measured from different channels and different tags by assigning each signal a different weight to enhance the direct-path signal and reduce the multipath

<sup>3</sup>RFID systems use frequency hopping for security reason.

<sup>4</sup>The baseline measurements only need to be measured once.



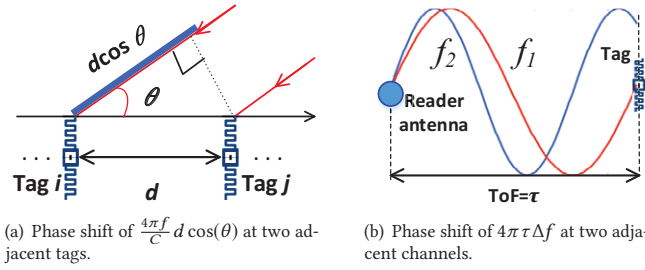


Figure 6: Phase shifts of measured direct-path signals at two adjacent tags and two adjacent channels.

effect. The intuition is that the direct-path signals measured at nearby tags and adjacent channels are similar. Thus, we can align these direct-path signals by compensating the phase shifts with carefully chosen weights. Then, we sum up the compensated signals so the direct-path signals are aligned and added constructively, while the reflected path signals are reduced to a small value.

Formally, we consider a tag-array with  $M$  tags and a reader working in frequency hopping mode across  $K$  adjacent channels. We take the first tag as the reference tag and the first channel with frequency  $f$  as the reference channel. The tags are placed with a distance of  $d$  and the frequency spacing between adjacent channels is  $\Delta f$ . There are two types of phase shifts in the direct-path signals. First, the phase shift between tags is due to the propagation distance difference. As shown in Fig. 6(a), when two direct-path signals arrive at the tags at a same angle-of-arrival (AoA)  $\theta$ , the two direct-path signals have a propagation distance difference of  $d \cos(\theta)$  and thus a phase difference of  $\frac{4\pi f}{C} d \cos(\theta)$ . Second, the phase shift between channels is due to the carrier frequency difference. As shown in Fig. 6(b), two direct-path signals with slightly different frequencies arrive at a same tag with a very similar propagation time  $\tau$ . Thus, the two direct-path signals have a phase shift of  $4\pi \tau \Delta f$ .

To model the multipath reflection signals, suppose there are  $P$  copies (one direct-path and  $P-1$  reflection paths) of a transmission, i.e.,  $S=[s_1, s_2, \dots, s_P]^T$ , arriving at the array from  $P$  different AoA angles  $\theta=[\theta_1, \theta_2, \dots, \theta_P]$  with  $P$  different time-of-flights (ToF)s  $\tau=[\tau_1, \tau_2, \dots, \tau_P]$ . For  $M$  tags and  $K$  channels, we have a total of  $M \times K$  measured signals. The measured signal  $x_{m,k}$  at  $m$ -th tag and  $k$ -th channel is:

$$x_{m,k} = \sum_{p=1}^P s_p \cdot e^{-j \cdot [\omega(m,k,\theta_p) + \mu(m,k,\tau_p)]}, \quad (2)$$

$$\omega(m,k,\theta_p) = \frac{4\pi[f + (k-1)\Delta f]}{C} (m-1)d \cos(\theta_p), \quad (3)$$

$$\mu(m,k,\tau_p) = 4\pi(k-1)\Delta f[\tau_p - \frac{(m-1)d \cos(\theta_p)}{C}], \quad (4)$$

where,  $\omega(m,k,\theta_p)$  and  $\mu(m,k,\tau_p)$  represent two types of phase shifts due to the propagation distance difference and the carrier frequency difference. With respect to the direct-path signal at the reference tag and the reference channel, the phase shifts of direct-path signal at  $m$ -th tag and  $k$ -th channel are calculated using Eq. (3) and Eq. (4). Thus, we can align the direct-path signals by compensating the calculated phase shifts for measured signals at all tags and all channels, so the direct-path signals have a same phase and thus can be added constructively. Specifically, the weight for

compensating the phase shift of signal  $x_{m,k}$  at  $m$ -th tag and  $k$ -th channel is:  $e^{j \cdot \omega(m,k,\theta_1)} \cdot e^{j \cdot \mu(m,k,\tau_1)}$ .

Without loss of generality, we assume  $s_1 \in S$  is the direct-path signal and  $\{s_2, \dots, s_P\}$  are the reflection-path signals. We can now sum the weighted signals as follows:

$$\begin{aligned} \Gamma &= \sum_{m=1}^M \sum_{k=1}^K x_{m,k} \cdot e^{j \cdot \omega(m,k,\theta_1)} \cdot e^{j \cdot \mu(m,k,\tau_1)} \\ &= \left( s_1 + \sum_{p=2}^P s_p \right) + \dots + \\ &\quad \left( s_1 + \sum_{p=2}^P s_p e^{j \cdot [\omega(M,K,\theta_1) - \omega(M,K,\theta_p) + \mu(M,K,\tau_1) - \mu(M,K,\tau_p)]} \right) \\ &= \underbrace{MK \cdot s_1}_{\text{Direct-path signal increased}} + \underbrace{\sum_{p=2}^P \left[ s_p \left( \sum_{m=1}^M \sum_{k=1}^K e^{j \cdot \Psi(m,k,\theta_p,\tau_p)} \right) \right]}_{\text{Reflection signals add up with random phase shifts}}, \end{aligned} \quad (5)$$

where,  $\Psi(m,k,\theta_p,\tau_p) = \frac{4\pi[f + (k-1)\Delta f](m-1)d}{C} [\cos(\theta_1) - \cos(\theta_p)] + 4\pi(k-1)\Delta f(\tau_1 - \tau_p)$ . As shown in the above equation, the direct-path signal  $s_1$  adds constructively and its power is increased by  $MK$  times. The reflection-path signals are relatively random, i.e., their angle  $\theta_p$  and propagation time  $\tau_p$  ( $p \neq 1$ ) are quite different from  $\theta_1$  and  $\tau_1$  of direct-path signal and are usually very different from each other. Thus, when we align the direct-path signals, the reflection signals add with random phases and their power averages out to a small value. Note that this “averaging out” happens when angles and propagation delays of different reflection signals are randomly distributed which is usually true in reality. With a relatively large value of  $M$  and  $K$ , the power of the combined direct-path signals is much stronger than the power of the reduced reflection-path signals. Thus, the direct-path signal now dominates and the linear relationship holds. We can then estimate the direct-path signal  $\hat{s}_1$ , and its corresponding phase  $\phi$  and RSS  $R$  as:

$$\hat{s}_1 \approx \Gamma / (MK), \quad \phi = \angle(\hat{s}_1), \quad R = 20 \log |\hat{s}_1|, \quad (6)$$

where  $\angle(\cdot)$  and  $|\cdot|$  represent the angle and absolute value of a complex number. In this paper, we employ the JADE [30] algorithm to jointly estimate the angle  $\theta_1$  and propagation time  $\tau_1$  of the direct-path signal. Specifically, JADE is a subspace-based technique which is an extension of the well known MUSIC algorithm [24]. MUSIC is utilized for one-dimensional parameter estimation while JADE is capable of multi-dimensional parameter estimation. We use the method introduced in SpotFi [15] to identify the direct path.

In the rest of this paper, we use the strengthened direct-path signal's phase and RSS value, i.e.,  $\phi$  and  $R$  in Eq. (6), for material identification and target imaging.

### 3.3 Target Material Identification

We first introduce the phase and RSS changes caused by a target and then describe our material identification method.

**Phase changes after a target shows up.** The wavelength of RF signal changes when the signal travels from one material into another while the frequency does not change [6]. As a result, the phase changes are different when the RF signal travels inside different materials, even if the propagation distances are the same. Considering the direct path between the reader and “Tag-array 1”

as shown in Fig. 4, where the RF signal penetrates through a target. Let  $L$  and  $L'$  denote the distances along the direct path from the reader to tag-array and to target, respectively.  $D$  is the propagation distance inside the target. Let  $\phi^{air}$  and  $\phi^{tar}$  be the measured signal phase before and after the target blocks the direct path. The phase change  $\Delta\phi = \phi^{tar} - \phi^{air}$  after the target shows up is given by:

$$\begin{aligned}\Delta\phi &= [2(L-D)\frac{2\pi}{\lambda_{air}} + 2D\frac{2\pi}{\lambda_{tar}} - 2L\frac{2\pi}{\lambda_{air}}] \bmod 2\pi \\ &= [2D(\frac{2\pi}{\lambda_{tar}} - \frac{2\pi}{\lambda_{air}})] \bmod 2\pi \\ &= [2D(\beta_{tar} - \beta_{air})] \bmod 2\pi,\end{aligned}\quad (7)$$

where  $\lambda_{air}$  and  $\lambda_{tar}$  are signal wavelengths in the air and in the target. The  $\beta_{air} = \frac{2\pi}{\lambda_{air}}$  and  $\beta_{tar} = \frac{2\pi}{\lambda_{tar}}$  are defined as the signal's phase constant in the air and in the target.

**RSS changes.** The RSS measurement also changes when the RF signal travels through different target materials. Specifically, the amplitude has an  $e^{-\alpha}$  attenuation over a unit propagation distance, where  $\alpha$  is the attenuation constant which only depends on the target material [6]. Let  $R^{air}$  and  $R^{tar}$  be the RSS measurements before and after the target blocks the direct path. Then, the RSS change  $\Delta R = R^{tar} - R^{air}$  is given as:

$$\begin{aligned}\Delta R &= 20\log\left(\frac{A_{tar}}{A_{air}}\right) \\ &= 20\log\left(\frac{A_S \cdot e^{-\alpha_{air}2L'} e^{-\alpha_{tar}2D} e^{-\alpha_{air}2(L-L'-D)}}{A_S \cdot e^{-\alpha_{air}2(L'+D+L-L'-D)}}\right) \\ &= 20\log[e^{-2D(\alpha_{tar}-\alpha_{air})}],\end{aligned}\quad (8)$$

where  $A^{air}$  and  $A^{tar}$  are the measured signal amplitudes before and after the target blocks the direct path,  $A_S$  is the amplitude of the transmitted signal,  $\alpha_{air}$  and  $\alpha_{tar}$  are the signal's attenuation constants in the air and in the target. Note that Eq. (7) and Eq. (8) also show that the distance  $L$  between tags and reader does not affect TagScan's performance, since it is cancelled out when calculating the phase change and RSS change measurements.

**3.3.1 Material feature extraction.** To identify the material type, we need to extract features that are uniquely related to the material. The phase and RSS changes can not be used directly, since they are also related to the target size, i.e., the propagation distance  $D$ . Compared with the phase and RSS changes, the phase constant  $\beta$  and attenuation constant  $\alpha$  are more promising candidates to serve as features for material identification. Different materials have different  $\beta$  and  $\alpha$  values [6]. However, it is a challenge to estimate the values of  $\beta$  and  $\alpha$  at the same time since there are three unknown parameters including the propagation distance  $D$  in the two equations Eq. (7) and Eq. (8). Employing multiple reader-tag pairs or frequency-hopping to increase the number of equations does not solve this problem, because the created additional equations are redundant. We address this problem with a novel method. Instead of seeking the absolute values of phase constant  $\beta$  and attenuation constant  $\alpha$ , we prove that the relative relationship of  $\beta$  and  $\alpha$  calculated by the RSS change and phase change is a parameter independent of target size, and also is unique for each material.

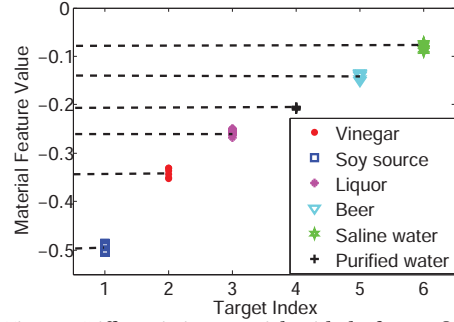


Figure 7: Differentiating materials with the feature  $\Omega$ .

Specifically, based on Eq. (7) and Eq. (8), we have:

$$2D = \frac{\Delta\phi + 2\zeta\pi}{\beta_{tar} - \beta_{air}} = \frac{\ln 10^{\Delta R/20}}{\alpha_{air} - \alpha_{tar}}, \quad (9)$$

where,  $\zeta$  is an integer.<sup>5</sup> Based on Eq. (9), we define a feature, i.e., RP-rate  $\Omega$ , which is related to the ratio of RSS change and phase change as:

$$\Omega = \frac{\ln 10^{\Delta R/20}}{\Delta\phi + 2\zeta\pi} = \frac{\alpha_{air} - \alpha_{tar}}{\beta_{tar} - \beta_{air}}. \quad (10)$$

Note that (i)  $\beta_{air}$  and  $\alpha_{air}$  are constants, since they are the phase constant and attenuation constant in the air; (ii) the values of  $\beta_{tar}$  and  $\alpha_{tar}$  are also fixed for a given material. Thus, the right side of Eq. (10) is a constant and  $\Omega$  is unique for a particular material. To this end, we successfully avoid solving  $\beta_{tar}$  and  $\alpha_{tar}$  but employ  $\Omega$  estimated by Eq. (10) for material identification. The feature  $\Omega$  is independent of the signal propagation distance inside a target which enables material identification without a need of knowing the target size. We show through benchmark experiments that  $\Omega$  is a fine-grained feature sensitive enough to identify different target materials. We test 6 liquid materials, i.e., "Vinegar", "Soy source", "Liquor", "Beer", "Saline water" and "Purified water". We conduct experiments in the lab-office environment based on the deployment shown in Fig. 1(a). We run the experiments 40 times and calculate the values of  $\Omega$  based on Eq. (10). The results in Fig. 7 show that the  $\Omega$  values of 6 liquids are clearly different from each other. It implies that  $\Omega$  can be employed to effectively identify the target's material type.

**3.3.2 Material identification.** TagScan has two steps for material identification. First, TagScan builds a feature database which maps the materials to feature ( $\Omega$ ) values. Specifically, for each material, we collect the phase and RSS change measurements in an open space, and then calculate its feature value according to Eq. (10). Note that this process happens only once. Second, based on the phase and RSS change measurements of a test material, TagScan calculates the new feature value and employs the KNN classifier [9] to identify the material type with the database.

**3.3.3 Distinguish between similar materials.** The feature value  $\Omega$  is a fine grained parameter to differentiate materials. We can even employ  $\Omega$  to differentiate Pepsi and Coke as shown in Section 5.3. In rare cases when the  $\Omega$  values are similar, the phase and RSS

<sup>5</sup>  $\zeta=0$  for relatively small objects. The propagation distance inside the water needs to be more than 84.25 cm to cause a phase change of more than  $2\pi$ .

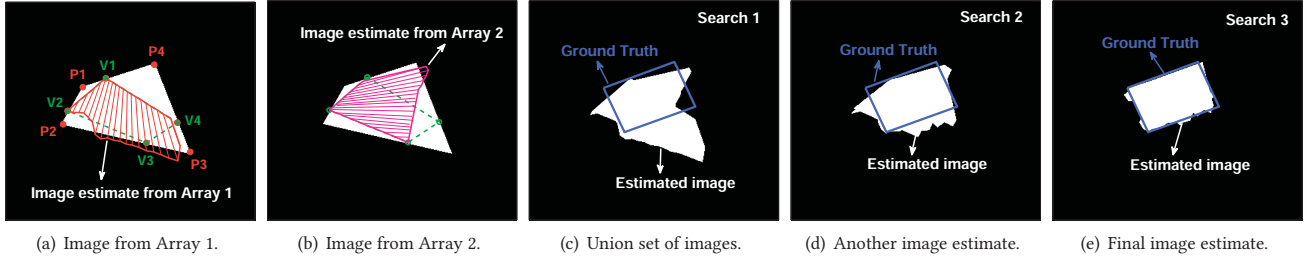


Figure 8: An illustration of target imaging. (a) and (b) show the target image estimates from Array 1 and Array 2, respectively. (c) is the union set of the two estimated images in (a) and (b). (d) shows another image estimate. (e) shows the output of final image estimate when the difference of images estimated from the two arrays is smaller than a pre-defined threshold.

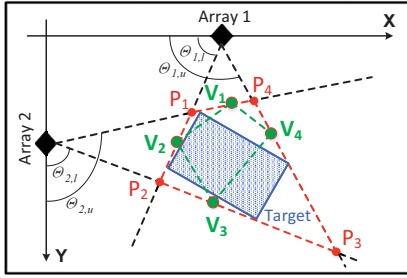


Figure 9: Boundary detection and starting points selection.

change values of each individual may be quite different and can also be employed to further differentiate two materials. For example, we find that sweet water with a 6% sugar concentration has a similar  $\Omega$  with Coke but their phase change values are very different.

**3.3.4 Propagation distance estimation.** After identifying the target's material, we can acquire the material's phase constant  $\beta$  either via experiment or from handbook [6]. Then, the propagation distance  $D$  can be estimated from Eq. (7) for imaging. We employ the phase measurement but not the RSS measurement to estimate  $D$  since the resolution of phase data is higher and the phase readings are usually more stable than the RSS readings.

### 3.4 Target Shape Imaging

TagScan utilizes the propagation distances inside a target for imaging. Specifically, each propagation distance represents one piece of target width information at one angle. By stitching together these width information at many angles, TagScan can obtain the horizontal cut image of the target. Note that TagScan can obtain the propagation distances at different angles after the target's material is identified. However, the challenge here is that we have no idea about the starting points of the propagation distances. To address this challenge, the key intuition is that the target images estimated by two different arrays will align well when the starting points are correctly selected. Thus, we model the imaging problem as an optimization problem and search the starting points by minimizing the difference of two images estimated from the two arrays.

To narrow down the search space, we first detect the angles of the target boundaries based on the phase change measurements. As shown in Fig. 9, TagScan detects the angles for the lower boundary  $\theta_{1,l}$  and the upper boundary  $\theta_{1,u}$  at "Array 1" by comparing the

phase changes with a threshold. However, the phase changes may be small when the target's boundary part is thin and the propagation distance inside the target is small. In this scenario, the phase noise will confuse the boundary detection. Traditionally, the Cumulative Sum (CUSUM) method [17] is used to address this type of boundary detection problem. However, this method needs a priori knowledge of the phase change distribution, which is not available in our design. To deal with this problem, we have two observations: (i) the phase variation caused by noise is random, which can be averaged out over a time window; (ii) phase changes caused by a target will be accumulated over the time window. We thus introduce a sliding window based cumulative phase change method to detect the angles of the target boundaries.

Formally, when the reader with antenna moves along a trajectory, let  $\{\Delta\phi_1, \dots, \Delta\phi_N\}$  be the phase changes at  $N$  successive angles  $\{\theta_1, \dots, \theta_N\}$  with respect to an array. If the indices of the lower and upper boundary angles are  $l$  and  $u$ , their corresponding estimated indexes  $\hat{l}$  and  $\hat{u}$  are:

$$\hat{l} = \inf\{n | J(n) > h\}, \quad \hat{u} = \sup\{n | J(n) > h\}, \quad (11)$$

$$J(n) = |V(n) - \frac{\sum_{i=1}^{n-1} V(n-i)}{n-1}|, \quad n \geq 2, \quad (12)$$

$$V(n) = \frac{1}{W} \sum_{j=n}^{n+W} \Delta\phi_j, \quad n \geq 1, \quad (13)$$

where,  $W$  is a robust window size used to reduce the false alarms,  $V(n)$  is the mean phase change of current window,  $J(n)$  calculates the difference between mean phase change values of the current window and the past windows,  $h$  is an empiric threshold defined for boundary detection.

Once the angles of the target boundaries are detected, we have a polygon formed by the four intersection points of the four angle boundaries obtained from two arrays, i.e., the polygon  $P_1P_2P_3P_4$  shown in Fig. 9. Next, TagScan estimates the target's cut image in the polygon area by searching the true starting points. Initially, TagScan randomly picks a point at each edge of the polygon  $P_1P_2P_3P_4$ , such as the points  $V_1, V_2, V_3$  and  $V_4$  in Fig. 9, and connects these points to form the initial candidate target edges. Then, each array chooses the closest candidate target edges and takes these edges as the *starting points* of the propagation distances estimated. For example, the "Array 1" chooses the edge  $V_1V_2$  and edge  $V_1V_4$  as the target edges and assumes the starting points are located on the two edges. TagScan can now stitch together the propagation



**Table 1: Test liquids for material identification.**

Liquids	Vinegar	Soy Source	Coke	Liquor	Beer
Compositions	Acetate 50%; Carbohydrate 4.9 g/100 ml.	Amino acids 0.4 g/100 ml; Carbohydrate 6.7 g/100 ml.	Carbohydrate 3.5 g/100 ml.	Ethyl alcohol 50% vol.	Ethyl alcohol 3.1% vol.
Liquids	Purified Water	Saline Water	Sweet Water	Whole Milk	Skimmed Milk
Compositions	—	Salt 10.9 g/100 ml.	Sugar 25.3 g/100 ml.	Fat 4.0 g/100 ml.	Fat 0 g/100 ml.

**Table 2: Test targets for cut imaging.**

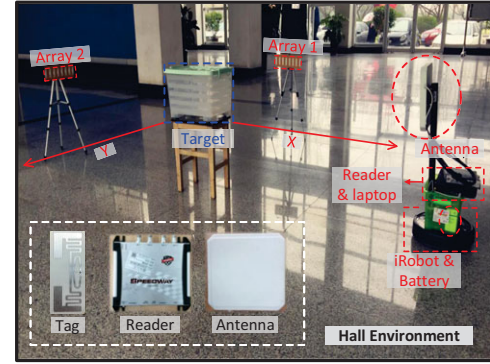
Horizontal cut of target	Size (cm)	Material
Triangular	Edge: 20	Plastic, wood, water.
Hexagonal	Edge: 20	
Quadrangular	43.5 × 34	
Quadrangular	81 × 81	Concrete.
Circular	Diameter: 25	Plastic, water.
Circular	Diameter: 20	
Human target	40 × 20	Water, fat, bone, etc.

distances along different angles and obtain the coarse estimated images with respect to the two arrays, as shown in Fig. 8(a)-(b).

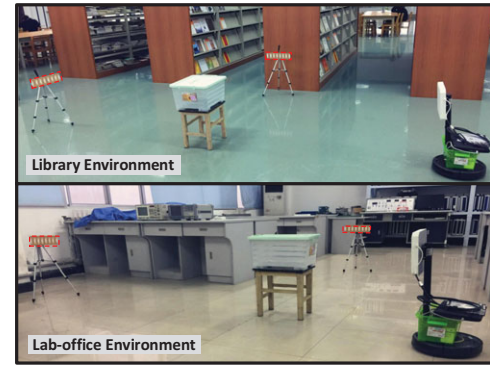
To combine the two images estimated from the two arrays, TagScan employs the union set of the two estimated images as the output. Fig. 8(c) shows the union set of two estimated images in Fig. 8(a)-(b). The estimated image in Fig. 8(c) is still quite different from the ground truth image which means the starting points of the propagation distances selected are not accurate. In reality, we do not know the ground truth so how can we know the estimated image is accurate? The key observation is that the images estimated from the two arrays will align well when all the starting points are selected accurately. While the starting points are located at the target edges, we search different combinations of target edge points on the four edges (e.g.,  $P_1P_2$ ,  $P_2P_3$ ,  $P_3P_4$  and  $P_4P_1$ ) and then calculate the difference between the two estimated images from the two arrays. For example, Fig. 8(c) and (d) show another two image estimates when we search two different combinations of target edge points. The image estimated in Fig. 8(d) is better than the image estimated in Fig. 8(c) since the difference between two estimated images is smaller. In reality, finding the minimum difference is not time efficient so as long as the difference is smaller than a pre-defined threshold, the search stops and the union set of the two images is output as the final target image estimate, as shown in Fig. 8(e). We utilize the MATLAB Genetic Algorithm toolbox to speed up this searching process. Based on the experimental results, the proposed imaging method can usually converge within one second and the average processing time is around 200 ms. Note that this method does not need to know if the target shape is triangle, rectangle or circle beforehand and will automatically use the propagation distances inside a target to determine the shape. However, we do find that the imaging performance of TagScan is worse for complex shapes such as a target with sawtooth edges.

## 4 IMPLEMENTATION

**Hardware implementation:** The system setup is shown in Fig. 10. An Impinj Speedway R420 reader [14] is employed in our experiments without any hardware or firmware modification. The R420 reader operates in frequency range of 920.625 – 924.375 MHz, which is divided into 16 channels with a channel bandwidth of 250 KHz. The default antenna used by R420 reader is a directional antenna with a 9 dBi gain and 70° elevation and azimuth beam widths. In



(a) Hall environment and system setup.



(b) Lab-office and library environment.

**Figure 10: System setup and experimental environments.**

the target imaging experiments, the reader together with the antenna is carried by an iRobot to move around the target for a half cycle. The moving speed is about 20 cm/s. Note that for material identification, we do not require the reader to move since the measurements at one location are enough. The cheap Alien General Purpose tags [12] are used in our experiments. Each tag costs 5 cents and is shown in Fig. 10(a). We place multiple tags (e.g., 8 tags) to form a linear tag-array and the spacing between adjacent tags is 4 cm. The heights of the tag-arrays and the reader antenna are the same, i.e., both of them are 44.5 cm above the ground.

**Backend implementation:** The proposed algorithms are implemented in C# and MATLAB code. The server is a laptop with a 2.6 GHz CPU (Intel i7-6700HQ) and 16 GB memory. The server communicates with the RFID reader using the low level reader protocol [13]. All the tags' backscatter packets received at the reader are forwarded to the server through an Ethernet cable. The size of the RFID backscatter packet is small (12 bytes) [14] since the packet only contains the tag's ID.



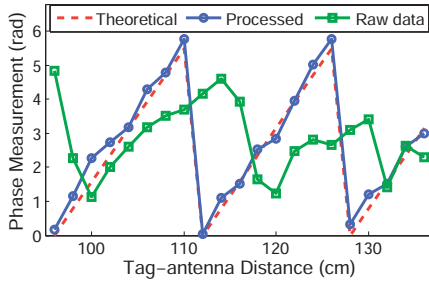


Figure 11: Phase change with the increasing distance between tag and antenna.

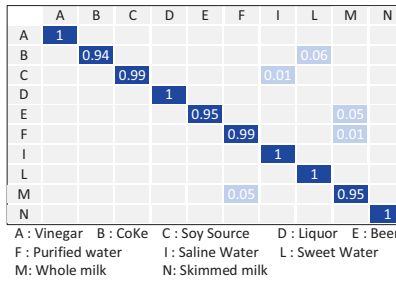


Figure 12: Confusion matrix: material identification results for the 10 liquids.

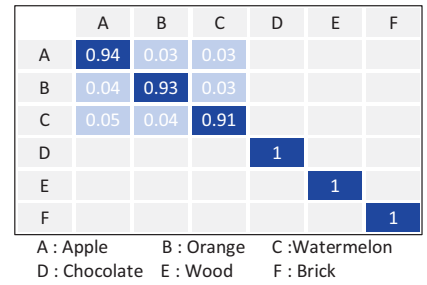


Figure 13: Confusion matrix: material identification results for the 6 solid targets.

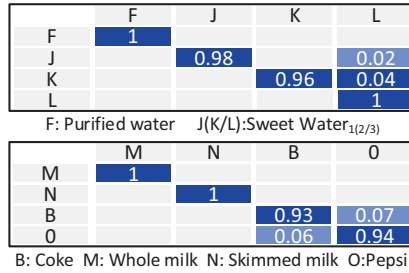


Figure 14: Confusion matrix: material identification results for the similar liquid materials.

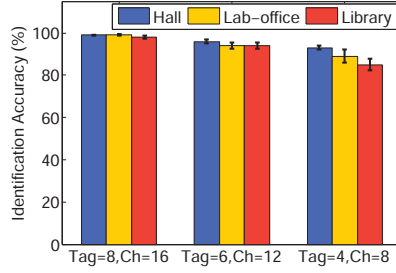


Figure 15: Material identification accuracy with varying number of tags and channels.

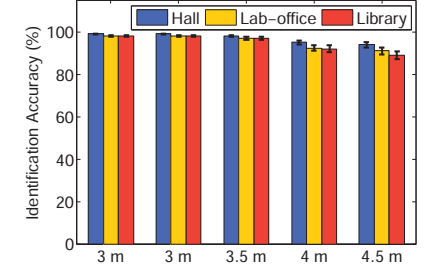


Figure 16: Material identification accuracy with varying tag-antenna distances.

**Default deployment setup:** In the experiment, we deploy one reader with one antenna and two tag-arrays. Each array has 8 tags for accurate AoA estimation [42]. The reader is programmed to hop over 16 channels. When we evaluate the impact of the number of tags and channels, we change the default setup. Unless specifically mentioned, we use this default setup for evaluation.

**Tag diversity calibration:** Accurate AoA estimation is highly dependent on the phase value measured from each tag. However, each tag has a random phase offset introduced by the hardware diversity [44] and the coupling effect [39]. This random phase offset needs to be carefully addressed before accurate AoA estimation. We employ the method proposed in [34] to calibrate the phase offsets among tags.

**System requirements:** In the current implementation, TagScan requires the target to be static for imaging. TagScan also requires the reader to move at a relatively low speed (i.e., below 0.5 m/s). When the reader moves fast, the Doppler shift effect will change the phase readings which will affect TagScan's performance accordingly.

## 5 PERFORMANCE EVALUATION

In this section, we evaluate the material identification and target imaging performance of TagScan. We first introduce the experimental environments and the tested targets, followed by the detailed experimental results.

### 5.1 Experimental Environments and Targets

**Experimental environments:** we conduct experiments in three typical indoor environments: a library, a lab-office, and an empty hall corresponding to high, medium and low multipath environments as shown in Fig. 10. For each experimental environment, we

choose a  $3.2 \text{ m} \times 3.2 \text{ m}$  area as the test area and deploy TagScan based on the layout shown in Fig. 4.

**Tested targets:** To evaluate the material identification performance of TagScan, we use 10 different liquids and 6 different types of solid objects as test targets. The liquids are listed in Table 1. The solid objects are "Apple", "Orange", "Watermelon", "Chocolate", "Wood" and "Brick". To evaluate the imaging performance of TagScan, we test targets with different shapes, sizes and materials. The details are shown in Table 2.

### 5.2 Effect of Multipath Suppression

In the lab-office environment, we deploy one reader with just one antenna and one tag-array. When the direct-path signal dominates, the phases change linearly with the distance between the tag-array and reader antenna. Fig. 11, shows that compared with the raw phase values, the processed values after applying the multipath suppression scheme have a linear pattern and match the theoretical values well. This demonstrates the effectiveness of the proposed multipath suppression scheme.

### 5.3 Material Identification Performance

**Material identification accuracy:** In the lab-office environment, we evaluate the material identification accuracy of TagScan. For each identification, we repeat the experiments 30 times by using 30 different targets with the same material, e.g., 30 apples of a same brand. For each target, we collect 100 samples and set the number of "Nearest Neighbors" as 12 in the KNN classifier based on our empirical knowledge. Fig. 12 shows the identification accuracy is more than 94% for 10 liquid materials. Fig. 13 shows the identification accuracy is also high for solid targets although the

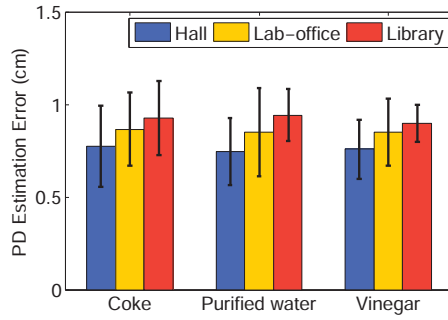


Figure 17: PD estimation errors in different environments.

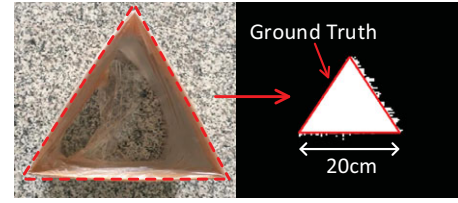
performance is slightly worse than liquids, since even two apples of the same brand have slightly different feature values. We run additional experiments to identify the same type of liquids with slightly different concentrations, e.g., sweet water with sugar concentration 8.3 g/100ml, 16.7 g/100ml and 25.3 g/100ml. Fig. 14 (up) shows that TagScan still achieves a high accuracy of at least 96%. Finally, we attempt to differentiate between “Coke”, “Pepsi”, “Whole milk” and “Skimmed milk”. Fig. 14 (below) shows that TagScan achieves 100% accuracies in differentiating the two types of milk since their phase difference is big as shown in Fig. 1(b). The difference between “Coke” and “Pepsi” is relatively small but TagScan still achieves a higher than 90% accuracy.

**Effect of the number of tags and channels:** More tags and channels are helpful to suppress the multipath and increase the phase estimation accuracy of direct-path signal. We run the material identification experiments on the 10 liquids with varying number of tags and channels in different environments. Fig. 15 shows that (i) the identification accuracy does increase with more tags and channels; (ii) even in a rich multipath environment such as a library, TagScan still achieves a high accuracy with 8 tags and 16 channels. This further demonstrates the effectiveness of the proposed multipath suppression scheme.

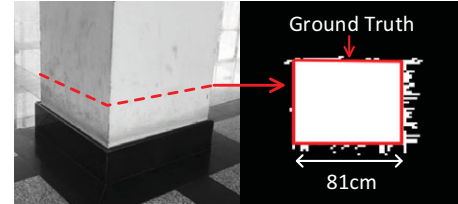
**Effect of the distance between antenna and tags:** When the distance between the antenna and the tag-array is larger, the signal becomes weaker and the multipath effect is stronger, which decrease the identification accuracy. We run material identification experiments on 10 liquids with varying distances between the antenna and the tag-array. Fig. 16 shows that the identification accuracy of TagScan does not decrease much. TagScan achieves an accuracy of higher than 90% in all the three environments when the tag-antenna distance is no larger than 4 m.

## 5.4 Shape Imaging Performance

**5.4.1 Accuracy of propagation distance estimation.** In this section, we evaluate the accuracy of the propagation distance (PD) estimation. Under the deployment setup shown in Fig. 1(a), we conduct experiments in the three environments using purified water, Coke and vinegar. We acquire the phase constant via the experimental measurement, i.e., we calculate the phase constant based on the phase value for a given liquid height. Fig. 17 shows that for a liquid target with a height of 10 cm, the mean propagation distance estimation errors are smaller than 1 cm.



(a) Imaging of a triangle shape target with plastic &amp; water.



(b) Imaging of a rectangular shape cement pillar.

Figure 18: Cut imaging of a triangular target and a rectangular target with material of plastic &amp; water and cement.

**5.4.2 Single target imaging.** Next, we evaluate TagScan’s imaging performance for the 7 targets listed in Table 2 in the lab-office environment. Fig. 18 demonstrates that TagScan can estimate the cut image of a triangular shape and a rectangular shape accurately with only two arrays. Fig. 18(b) also shows that TagScan achieves a high accuracy when the target material is cement.

When the cut shape of the target is a hexagon or a circle, the imaging performance of TagScan degrades as shown in Fig. 19(a)-(b), because the constraints (i.e., the propagation distances) from the two arrays are not enough to achieve a fine-grained image. To achieve a better accuracy, we increase the number of arrays from 2 to 4. As shown in Fig. 19(c), the imaging performance improves significantly with more arrays. However, the computational load also increases with more arrays.

**5.4.3 See-through the wall imaging.** Next, TagScan is tested to image one and two targets behind a wall made of plywood.<sup>6</sup> We first carry out one round of baseline measurements when there is no target behind the wall. Then, TagScan performs another round of measurements when the target appears behind the wall and estimates the cut image of the target. Fig. 20(a) shows that the wall is not affecting the imaging performance and TagScan still accurately obtains the target image behind a wall.

**5.4.4 Human target imaging.** We test if TagScan can accurately obtain the cut image of a human target as this information can be employed for human identification. However, estimating the propagation distance inside a human body is more challenging, as the human body is composed of different materials that are in both liquid and solid forms. To overcome this challenge, TagScan first calculates the average phase constant using 15 different human targets (all volunteers are from the lab). Then, one human target is randomly selected for the imaging evaluation. Fig. 20(b) shows that TagScan can estimate the cut image of a human body at a relatively

<sup>6</sup>The thickness of the plywood wall is about 6 cm for easy of construction but the RFID signal can penetrate through a much thicker wall as demonstrated in Fig. 18(b).

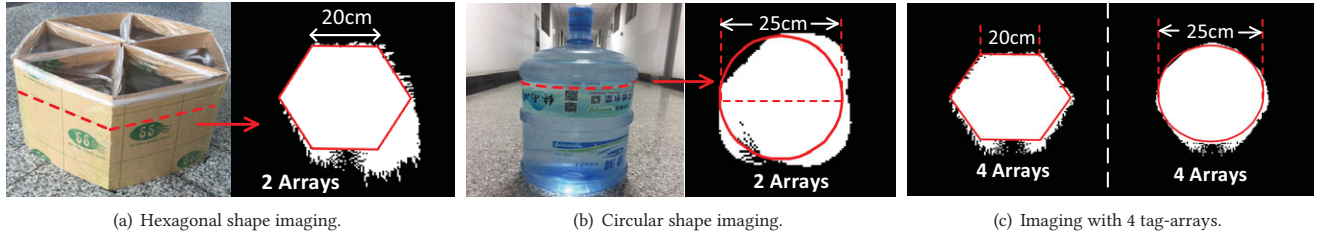


Figure 19: Cut imaging for a hexagonal target and a circular target with two and four arrays.

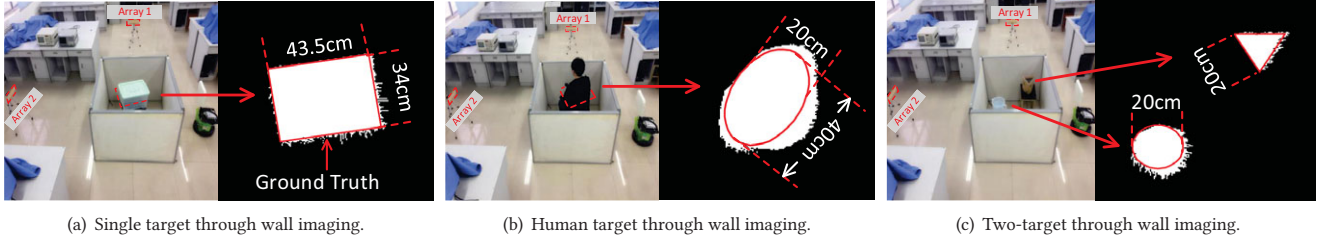


Figure 20: See-through wall imaging for a single target, human target and two targets.

high accuracy. Note that a person's different clothes on different days may lead to small changes in estimated cut image. For the current experiments, the human target wears the same cloth.

**5.4.5 Two-target imaging.** Finally, TagScan is evaluated in a challenging scenario where there are two targets. The intuition allows TagScan to succeed is that the two targets will affect the direct-path links separately when the targets are not located close to each other. In this case, as shown in Fig. 20(c), TagScan images both targets accurately. When targets are very close to each other, TagScan will image them as one large target.

## 6 DISCUSSION

**Maximum propagation distance inside a target:** The transmission power of a COTS RFID reader is limited to 32.15 dBm and the weakest signal power that a reader can hear is around -90 dBm [14]. We measure and find that the maximum propagation distance that a RFID reader can still read a signal sent back by a tag through purified water is around 4 m. However, this is not a fundamental limitation of TagScan but the limit of hardware. By using directional antenna with thinner transmission beam, TagScan should have no problem for imaging even larger target.

**Target mobility:** When a target is moving, TagScan can still identify its material as long as the target passes through the direct-path link formed by the tag-array and the reader antenna. However, it is challenging to estimate a moving target's image since TagScan needs to match the baseline phase/RSS readings (without the target) with the online measurements (with the target) at the exact same target location to calculate the phase/RSS changes. When the target is moving, it is difficult to match the measurements with the appropriate baseline values.

**End-to-end system latency:** The system latency includes data collection time and the processing time of the algorithms to identify the material and image the target. The processing time is around

50 ms for material identification and 200 ms for imaging. For material identification, TagScan needs one round of measurements over 16 channels, which takes about 350 ms. Thus, the latency is below 0.5 s. The packet collection time for imaging depends on the size of the monitoring area. For example, TagScan takes 40 s to collect packets in a 4 m × 4 m area when the robot moves around the target for a half cycle at a speed of 20 cm/s. The data collection rate of the Impinj R420 reader is about 45 samples per second. So the number of samples collected for imaging is about 1800.

**Identifying hybrid materials.** In reality, a lot of targets consist of hybrid materials. It is a challenging problem to identify each component material and the corresponding percentage. We leave this interesting problem as the future work.

**Imaging hollow targets.** Imaging hollow targets has a lot of applications but is also challenging for TagScan. With holes inside the target, one propagation distance obtained may be divided into several segments which makes imaging much more difficult.

**Impact of container on material identification.** In the current experiments, the empty container (i.e., cup) is included when we carry out the baseline measurements. Thus, the effect caused by the container is totally removed, i.e., the material and the thickness of the container will not affect the identification of the internal material. In real-life applications, we may not always have the chance to carry out baseline measurement with the empty container beforehand. In these scenarios, the container's material and thickness do affect TagScan's performance.

## 7 RELATED WORK

**Commodity imaging systems.** These systems including Radar[19], X-Ray[21], CT/MRI [49] and B-scan [7], employ dedicated hardware with high frequencies, large bandwidths and antenna arrays, which are extremely expensive and usually large in size. For example, a medical MRI system [49] can cost 200000-1000000 USD. MRI [49] requires the target to be placed inside a large coil and then uses the resonance signal reflected by the target for imaging. Moreover,



X-Ray and CT employ very high frequency signals which are harmful to the human body [23]. The ultrasonic systems, like B-scan [7], can only work within a short distance range (e.g., sub-meters) and are easily disrupted by the background noise. TagScan is built on cheap commodity RFID devices (around 1000 USD) that works for a relatively long distance range of 10 meters.

**Camera and infrared based systems.** Thermal infrared sensor or visible light camera is widely used for target imaging [48] and material identification [4, 20, 27]. Specifically, they acquire a target's millions of reflectance and/or fluorescence spectra for material identification [4]. The thermal infrared sensor works in the night but it requires the target to have a temperature above a specific threshold to be detected. The visible light camera requires good lighting conditions and has privacy issues. Moreover, both of them cannot work in non-line-of-sight scenarios where the target is blocked from line-of-sight (LoS) view. TagScan has the advantages of working at day and night, not affected by heat sources, and can also penetrate non-metallic walls.

**RF-based imaging systems.** Previous imaging work relies on RF tomography technique [2, 41, 45]. However, they only obtain a very coarse-grained image and do not capture the target's fine-grained shape information. The RF-Capture system [1] captures the coarse skeleton information of a human target behind a wall using 20 antennas with a 1.78 GHz bandwidth. In contrast, TagScan is built using low-cost commodity RFID devices and only requires one antenna and a 4 MHz bandwidth. The Wision [11] system based on Wi-Fi infrastructure requires a large two-dimensional antenna array and uses the reflected signals from a target for imaging. Its imaging performance is coarse due to the small bandwidth of commodity Wi-Fi devices. Moreover, all the above systems only obtain the vertical cut image and the surface material of a target, since they use the reflection signals bounced off the target. TagScan uses the signals that penetrate through a target and thus is able to obtain the horizontal cut image and the internal material of the target. Depatla *et al.* [8] build a Wi-Fi imaging system by using the RSS attenuation caused by a target. However, the RSS readings from Wi-Fi cards are coarse, limiting its imaging accuracy. It also requires two Wi-Fi transceivers to move simultaneously and know each other's position at all time, severely limiting its practical application. TagScan only needs one moving antenna and uses much more fine-grained phase information for imaging.

**RF-based material identification systems.** The RSA system [50] uses 60 GHz radios to identify a nearby target's surface material and image its boundaries. However, 60 GHz signals have a short transmission range and require LoS view to the target. On the contrary, the wavelength of the RFID signal is relatively large (i.e., about 32 cm), which allows TagScan to identify a target's material and image its shape through a wall. RadarCat [46] also uses 60 GHz signals for accurate material and object classification. However, RadarCat requires to touch the target, which may not be convenient in some scenarios. While, TagScan can passively identify a target's material even when the target is away (1-5 m) from the devices (i.e., tag and antenna). Moreover, RFID's frequency band is much smaller than the 60 GHz signal. As a result, the sampling interval is much larger and the distance estimate is coarse. Thus, it is more challenging to carry out imaging and material identification with RFID signals. Sarma *et al.* [5] build an RFID based liquid volume

detection system by mapping the RSS measurements with the level of liquid in the glass. However, this system can not identify the liquid material. TagScan not only can identify the target material, but also can estimate the liquid height accurately.

**Multipath suppression approaches.** Many methods have been proposed to address the multipath problem indoors [2, 15, 29, 42, 43]. ArrayTrack [42] employs the property that the direct path is more stable when the target is moving to identify the direct path. Chronos [29], ToneTrack [43] and WiTrack [2] identify the ToF of the direct-path signal based on the property that ToF of direct path has the minimum value. Specifically, they either combine the Wi-Fi signals of multiple channels [43] or use the FMCW signal with a large bandwidth (i.e., sweeping from 5.46 GHz to 7.25 GHz) [2] to separate different signals in the time domain. SpotFi [15] combines the two ideas and identifies the AoA and ToF of direct-path signal at the same time. Unlike previous methods that extracting the AoA or ToF information to identify the direct-path signal, this paper tries to strengthen the direct-path signal and average out the multipath signals. So our method is actually able to obtain the raw direct-path signal rather than just differentiating which AoA/ToF is corresponding to the direct-path signal.

## 8 CONCLUSION

This paper presents TagScan, the first RFID-based system which utilizes the phase and RSS changes to perform material identification and target imaging at the same time. Comprehensive real-world experiments show that TagScan can achieve high accuracies for target material identification and is sensitive enough to differentiate even Pepsi and Coke. TagScan can also image more than one targets of different shapes, sizes behind a wall.

## ACKNOWLEDGMENT

This work is supported by National Natural Science Foundation of China (61572402, 61672428, 61672427). This research is also supported by the National Research Foundation, Prime Minister's Office, Singapore under its IDM Futures Funding Initiative. We also would like to thank the shepherd Prof. Lili Qiu, as well as Prof. Baochun Li and the anonymous reviewers for their valuable feedbacks on this paper. Xiaojiang Chen and Dingyi Fang are the corresponding authors.

## REFERENCES

- [1] Fadel Adib, C Hsu, Hongzi Mao, Dina Katabi, and Fredo Durand. 2015. Capturing the human figure through a wall. *ACM Transactions on Graphics* 34, 6 (2015), 219–231.
- [2] Fadel Adib, Zach Kabelac, Dina Katabi, and Robert C Miller. 2014. 3d tracking via body radio reflections. In *Proc. USENIX NSDI*. 317–329.
- [3] Fadel Adib and Dina Katabi. 2013. See through walls with WiFi. In *Proc. ACM SIGCOMM*. 75–86.
- [4] Costas Balas, George Epitropou, Athanasios Tsapras, and Nikos Hadjicicolaou. 2016. A novel hyperspectral camera and analysis platform for the non-destructive material identification and mapping: An application in paintings by El Greco. In *IEEE International Conference on Imaging Systems and Techniques*. 211–215.
- [5] Rahul Bhattacharyya, Christian Floerkemeier, and Sanjay Sarma. 2010. RFID tag antenna based sensing: Does your beverage glass need a refill?. In *IEEE International Conference on RFID*. 126–133.
- [6] K Cheng David. 1983. Field and wave electromagnetics. *Addison-Wesley publications* (1983).
- [7] Bats F De, B Wolff, M Mauget-Faysse, C Scemama, and L Kodjikian. 2013. B-scan and "en-face" spectral-domain optical coherence tomography imaging for the

- diagnosis and followup of acute retinal pigment epitheliitis. *Case Reports in Medicine* 13, 2 (2013), 260–237.
- [8] Saandeep Depatla, Lucas Buckland, and Yasamin Mostofi. 2015. X-Ray Vision With Only WiFi Power Measurements Using Rytov Wave Models. *IEEE Trans. on Vehicular Technology* 64, 4 (2015), 1376–1387.
  - [9] Gongde Guo, Hui Wang, David Bell, Yaxin Bi, and Kieran Greer. 2003. *KNN Model-Based Approach in Classification*. Springer Berlin Heidelberg, 986–996 pages.
  - [10] Jinsong Han, Ding Han, Qian Chen, Dan Ma, Xi Wei, Zhi Wang, Zhiping Jiang, and Longfei Shangguan. 2014. CBID: A Customer Behavior Identification System Using Passive Tags. In *Proc. IEEE ICNP*. 47–58.
  - [11] Donny Huang, Rajalakshmi Nandakumar, and Shyamnath Gollakota. 2014. Feasibility and limits of wi-fi imaging. In *Proc. ACM SenSys*. 266–279.
  - [12] Alien Inc. 2008. Alien Tags. (mar 2008). Retrieved June 27, 2017 from <http://www.Alientechnology.com/tags/>
  - [13] EPCglobal Inc. 2007. Low Level Reader Protocol, Version 1.0. 1. (2007).
  - [14] Impinj Inc. 2010. R420 Readers. (mar 2010). Retrieved June 27, 2017 from <http://www.Impinj.com/products/readers/>
  - [15] Manikanta Kotaru, Kiran Joshi, Dinesh Bharadia, and Sachin Katti. 2015. Spotfi: Decimeter level localization using wifi. In *Proc. ACM SIGCOMM*. 269–282.
  - [16] Kyle Jamieson Longfei Shangguan. 2016. Leveraging Electromagnetic Polarization in a Two-Antenna Whiteboard in the Air. In *Proc. ACM CoNEXT*. 443–456.
  - [17] James M Lucas and Michael S Saccucci. 1991. Exponentially weighted moving average control schemes: Properties and enhancements. *Quality Engineering* 36, 1 (1991), 31–32.
  - [18] G Marin, F Dominio, and P Zanuttigh. 2014. Hand gesture recognition with leap motion and kinect devices. In *Proc. IEEE International Conference on Image Processing*. 1565–1569.
  - [19] S. M. J Mortazavi, S Taeb, and N Dehghan. 2013. Alterations of visual reaction time and short term memory in military radar personnel. *Iranian Journal of Public Health* 42, 4 (2013), 428–435.
  - [20] Susmit Nanda, Sourav Manna, Arup Kumar Sadhu, Amit Konar, and Diptendu Bhattacharya. 2015. Real-time surface material identification using infrared sensor to control speed of an arduino based car like mobile robot. In *International Conference on Computer, Communication, Control and Information Technology*. 210–216.
  - [21] Koichi Ogawa, Tsuma Hirokawa, and Shota Nakamura. 2010. Identification of a material with a photon counting x-ray CT system. In *IEEE Nuclear Science Symposium Conference Record*. 2582–2586.
  - [22] Qifan Pu, Sidhant Gupta, Shyamnath Gollakota, and Shwetak Patel. 2013. Whole-home gesture recognition using wireless signals. In *Proc. ACM MobiCom*. 27–38.
  - [23] Savithiri Ratnapalan, Yedidia Bentur, and Gideon Koren. 2008. Doctor, will that x-ray harm my unborn child? *Canadian Medical Association Journal* 179, 12 (2008), 1293–1296.
  - [24] Ralph O Schmidt. 1986. Multiple emitter location and signal parameter estimation. *IEEE Trans. on Antennas and Propagation* 34, 3 (1986), 276–280.
  - [25] Longfei Shangguan and Kyle Jamieson. 2016. The Design and Implementation of a Mobile RFID Tag Sorting Robot. In *Proc. ACM MobiSys*. 31–42.
  - [26] Longfei Shangguan, Zimu Zhou, Xiaolong Zheng, Lei Yang, Yunhao Liu, and Jinsong Han. 2015. ShopMiner: Mining Customer Shopping Behavior in Physical Clothing Stores with COTS RFID Devices. In *Proc. ACM SenSys*. 113–125.
  - [27] Juraj Števek, Svetozár Katusčák, Lenka Dubinyová, and Miroslav Fikar. 2016. An automatic identification of wood materials from color images. In *Cybernetics & Informatics (K&I)*. 111–116.
  - [28] Li Sun, Souvik Sen, Dimitrios Koutsonikolas, and Kyu-Han Kim. 2015. WiDraw: Enabling Hands-free Drawing in the Air on Commodity WiFi Devices. In *Proc. ACM MobiCom*. 77–89.
  - [29] Deepak Vasisht, Swarun Kumar, and Dina Katabi. 2016. Decimeter-level localization with a single WiFi access point. In *Proc. USENIX NSDI*. 165–178.
  - [30] A. J. Van Der Veen, M. C. Vanderveen, and A. Paulraj. 1997. SI-JADE: an algorithm for joint angle and delay estimation using shift-invariance properties. In *Proc. Signal Processing Advances in Wireless Communications*. 161–164.
  - [31] Ju Wang, Hongbo Jiang, Jie Xiong, Kyle Jamieson, Xiaojang Chen, Dingyi Fang, and Binbin Xie. 2016. LiFS: Low Human-Effort, Device-Free Localization with Fine-Grained Subcarrier Information. In *Proc. ACM MobiCom*. 243–256.
  - [32] Jue Wang and Dina Katabi. 2013. Dude, where's my card? RFID positioning that works with multipath and non-line of sight. In *Proc. ACM SIGCOMM*. 51–62.
  - [33] Jue Wang, Deepak Vasisht, and Dina Katabi. 2014. RF-idraw: virtual touch screen in the air using rf signals. In *Proc. ACM SIGCOMM*. 235–246.
  - [34] Ju Wang, Jie Xiong, Hongbo Jiang, Chen ? Xiaojang, and Dingyi Fang. 2016. D-Watch: Embracing "bad" Multipaths for Device-Free Localization with COTS RFID Devices. In *Proc. ACM CoNEXT*. 413–425.
  - [35] Wei Wang, Alex X Liu, Muhammad Shahzad, Kang Ling, and Sanglu Lu. 2015. Understanding and Modeling of WiFi Signal Based Human Activity Recognition. In *Proc. ACM MobiCom*. 65–76.
  - [36] Wei Wang, Alex X Liu, and Ke Sun. 2016. Device-free gesture tracking using acoustic signals. In *Proc. ACM MobiCom*. 82–94.
  - [37] Yan Wang, Jian Liu, Yingying Chen, Marco Gruteser, Jie Yang, and Hongbo Liu. 2014. E-eyes: device-free location-oriented activity identification using fine-grained wifi signatures. In *Proc. ACM MobiCom*. 617–628.
  - [38] Yuxi Wang, Kaishun Wu, and Lionel M Ni. 2016. WiFall: Device-free Fall Detection by Wireless Networks. *IEEE Trans. on Mobile Computing* 12, 5 (2016), 11–22.
  - [39] Teng Wei and Xinyu Zhang. 2016. Gyro in the air: tracking 3D orientation of batteryless internet-of-things. In *Proc. ACM MobiCom*. 55–68.
  - [40] William B Weir. 1974. Automatic measurement of complex dielectric constant and permeability at microwave frequencies. *Proc. IEEE* 62, 1 (1974), 33–36.
  - [41] Joey Wilson and Neal Patwari. 2011. See-through walls: Motion tracking using variance-based radio tomography networks. *IEEE Trans. on Mobile Computing* 10, 5 (2011), 612–621.
  - [42] Jie Xiong and Kyle Jamieson. 2013. ArrayTrack: a fine-grained indoor location system. In *Proc. USENIX NSDI*. 71–84.
  - [43] Jie Xiong, Karthikeyan Sundaresan, and Kyle Jamieson. 2015. ToneTrack: Leveraging frequency-agile radios for time-based indoor wireless localization. In *Proc. ACM MobiCom*. 537–549.
  - [44] Lei Yang, Yekui Chen, Xiang Yang Li, Chaowei Xiao, Mo Li, and Yunhao Liu. 2014. Tagoram: real-time tracking of mobile RFID tags to high precision using COTS devices. In *Proc. ACM MobiCom*. 237–248.
  - [45] Lei Yang, Qiongzhen Lin, Xiangyang Li, Tianci Liu, and Yunhao Liu. 2015. See Through Walls with COTS RFID System. In *Proc. ACM MobiCom*. 487–499.
  - [46] Huishyong Yeo, Gergely Flamich, Patrick Schrempf, David Harrisbirtill, and Aaron Quigley. 2016. RadarCat: Radar Categorization for Input and Interaction. In *Proc. ACM UIST*. 833–841.
  - [47] Moustafa Youssef, Matthew Mah, and Ashok Agrawala. 2007. Challenges: device-free passive localization for wireless environments. In *Proc. ACM MobiCom*. 222–229.
  - [48] Zhengyou Zhang. 2012. Microsoft Kinect Sensor and Its Effect. *IEEE Multimedia* 19, 2 (2012), 4–10.
  - [49] Hua Zhou, Yi Xiang J. Wang, Haiyan Lou, Xiaojun Xu, and Minming Zhang. 2014. Hepatic Sinusoidal Obstruction Syndrome Caused by Herbal Medicine: CT and MRI Features. *Korean Journal of Radiology* 15, 2 (2014), 218–225.
  - [50] Yanzi Zhu, Yibo Zhu, Ben Y. Zhao, and Haitao Zheng. 2015. Reusing 60GHz Radios for Mobile Radar Imaging. In *Proc. ACM MobiCom*. 103–116.